



Optimization of Medical CT Data with High Precision

Jing Chi¹ and Caiming Zhang¹

¹Shandong University of Finance and Economics, peace_world_cj@hotmail.com; czhang@sdu.edu.cn

ABSTRACT

The precision of medical CT data has an important effect on the CT image reconstruction precision. In this paper, we present a novel approach for optimizing the raw CT data acquired by scanner. The approach can effectively improve the raw CT data precision, and consequently, improve the reconstruction precision. The new approach is based on the fact that the raw CT data can be regarded as the area samples of human density, and the point samples are more accurate than the area samples. The new approach transforms the raw area samples to more accurate point samples to improve the CT data precision by three steps: 1) establish the mapping relationship between area samples and point samples; 2) Segment the raw CT slice into different regions based on the human tissue feature; 3) in each segmented region, construct quadric spline fitting equation with the mapping relationship to transform the area samples to more accurate point samples. Experiments show that the image reconstruction with the new data optimized by our method has more details and fewer artifacts.

Keywords: computerized tomography, precision optimization, quadric spline.

DOI: 10.3722/cadaps.2013.17-31

1 INTRODUCTION

Computer tomography (CT) is the gold standard in the diagnosis of large numbers of different disease entities. CT produces a volume of data which can be used for 2D or 3D medical reconstruction, in order to demonstrate various structures based on their ability to block the X-ray beam. CT allows doctors to inspect the inside of body without operating or performing unpleasant examinations. The 3D virtual human model reconstructed with CT data can help doctor pinpoint lesion sites and plan treatment. Moreover, combination of 3D model and virtual reality technology can help doctor simulate the surgical plan before operation. Obviously, as an assistant method, the quality of CT image reconstruction is very important to clinical diagnosis. Therefore, utilizing the information provided by CT data to achieve high precise and realistic reconstruction has become one of the basic problems in

medical image processing. Research of the problem has great significance for improving clinical diagnosis rate and success rate of operation.

The CT data is generated by detecting and measuring the strength of X-rays that have passed through the human body. Because the densities of body tissues are different, their abilities of absorbing X-rays are different. When X-rays pass through a certain body level composed of many small cubes with the same volume, known as voxels, the mean attenuation of each voxel, i.e., density value, is computed. The density value is called pixel. The pixels are arranged in matrix to form raw CT slice [2],[10]. From the generation of CT data, it can be seen that each pixel on raw CT slice is the average density of its corresponding voxel, that is, the pixel is area sample, not accurate point sample.

In recent years, many research results in medical image processing have been developed. [19] designs function and derivative reconstruction filters in volume visualization based on the spatial reconstruction smoothness and the spatial reconstruction error. [18] compares various interpolation methods, e.g., truncated and windowed sinc, nearest neighbor, linear, quadratic, cubic B-spline, cubic, Lagrange, and Gaussian, used for medical image generation and processing such as compression or resampling. [13] introduces and advocates the use of generalized interpolation in medical imaging, which involves a prefiltering step when correctly applied. Compared to traditional interpolations in [18], generalized interpolation not only performs better in the context of image transformations, but also comes a lower computational cost. [6] presents an objective task-specific framework for evaluating interpolation methods, and establishes shape-based and object-based methods in medicine for slice interpolation of three-dimensional data sets. [17] develops 2-D, nonseparable, piecewise cubic convolution (PCC) for image interpolation, but the 2-D PCC yields small improvements in interpolation fidelity over the traditional, separable methods. [16] uses edge information to guide the reconstruction of a skeleton image structure and the interpolation that follows. [23] proposes a soft-decision interpolation technique to estimate missing pixels in groups rather than one at a time. The technique preserves spatial coherence of interpolated images better than traditional interpolations. [3] investigates effect of applying different types of wavelet filters belonging to orthogonal and biorthogonal families with different orders on the medical image quality in multi-resolution framework. [4] introduces 33 topologically different configurations in Marching Cubes algorithm to construct topologically correct isosurfaces in surface rendering. [9] completes the algorithm in [4] for the ambiguity resolution and for the feasibility of the implementation. [21],[14] respectively introduce mesh simplification and image segmentation in Marching Cubes algorithm to improve the efficiency of 3D medical image reconstruction. [12] presents a shear-warp algorithm that is one of the fastest algorithms for volume rendering, but the expressive speed comes at the price of reduced image quality. [7],[8] improve the precision of shear-warp algorithm while still maintain reasonable rendering speed. [22] proposes a method for direct volume rendering based on segmenting a volume into regions of equivalent contour topology and applying separate transfer functions to each region. The method has high efficiency and is hardware-accelerated. [1] develops faster and higher quality volume visualization techniques for 3D medical imaging by directly processing the sensor data acquired with scanner, rather than the image data reconstructed from the sensor data. [15] proposes a regularized interpolation method that improves the reconstruction quality by specifying a tradeoff between fidelity to the medical image data and robustness to the noise. [20] presents an automatic algorithm for surface rendering of a volume consisting of multi-axial cross sections. The 3D images obtained from multi-axial volumes are more clinically useful than those obtained from one-axial volumes.

All the aforementioned methods use the raw CT data for image reconstruction and processing. They do not take into account the effect of the precision of the raw CT data per se on the quality of the image reconstruction and processing. The raw CT data are area samples in nature, not accurate point samples. Using directly these area samples for image reconstruction or processing may loss some

details information. Thus, in this paper, we focus on improving the precision of the raw CT data per se. By optimizing the raw CT data, i.e., transforming the area samples to more accurate point samples, we can efficiently improve the precision of the CT data. When image reconstruction or processing algorithms are conducted on the CT data after optimization, the reconstruction and processing precisions are naturally improved since the CT data after optimization are more accurate.

2 NEW PRECISION OPTIMIZATION APPROACH

We present a novel approach for optimizing the raw CT data precision. The new approach can get more accurate approximations of point samples from the area samples on raw CT slice. Using these new optimized data with high precision for 2D and 3D reconstruction, the quality will be effectively improved. The novel approach first establishes the mapping relationship between area samples and point samples, then segments the CT slice into different regions based on human tissue feature, and finally, in each segmented region, constructs quadric spline fitting equations based on the mapping relationship to transform the area samples to more accurate approximations of point samples.

2.1 The Mapping Relationship between Area Samples and Point Samples

All pixels on raw CT slice are area samples. Assuming that there are l slices of CT data, and $n \times n$ pixels on each slice, then these $n^2 l$ pixels can be regarded as area samples obtained from a continuous human volume space in $n^2 l$ unit cubes (i.e., voxels). In reconstruction, these samples are used to build fitting model to approximate the original human volume space. Obviously, the more precise the samples are, the higher the approximation accuracy of the fitting model is. Therefore, if precise point samples can be got from area samples, and used for reconstruction, the model precision will be improved. In fact, it is nearly impossible to get precise point samples from area samples, so we get approximations of point samples with high accuracy in our approach. The mapping relationship between area samples and point samples is established first.

In one-dimensional case: As shown in Fig.1, let $P(x)$ be a curve, and $F_i, i = 0, 1, \dots, n-1$ be n area samples (denoted by blue dot) obtained from $P(x)$ with respect to regions $[x_i, x_{i+1}]$, then, according to the definition of definite integral, in each region $[x_i, x_{i+1}]$, the definite integral $\int_{x_i}^{x_{i+1}} P(x) dx$ can be evaluated approximately in terms of the area of the rectangle whose length and width is respectively the length of $[x_i, x_{i+1}]$ and F_i , i.e., in terms of the product of the length of $[x_i, x_{i+1}]$ and F_i . So the following relationship is satisfied

$$\int_{x_i}^{x_{i+1}} P(x) dx = F_i \cdot L_i, \quad i = 0, 1, \dots, n-1 \quad (2.1)$$

Where, $L_i = |x_{i+1} - x_i|$, is the length of the region $[x_i, x_{i+1}]$. We can use $P_i, i = 0, 1, \dots, n-1$ as fitting points to get approximate expression of $P(x)$, and consequently, establish the mapping relationship between area samples F_i and point samples $P_i, i = 0, 1, \dots, n-1$ in Eqn.(2.1). The computed $P_i, i = 0, 1, \dots, n-1$ from Eqn. (2.1) are the approximations of point samples on the curve $P(x)$.

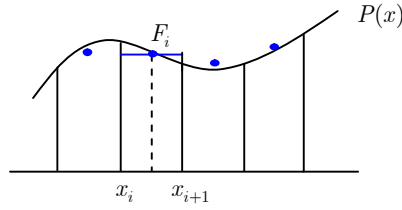


Fig. 1: Illustration of the mapping relationship in one-dimensional case.

In two-dimensional case: let $P(x, y)$ be a surface, and $F_{ij}, i, j = 0, 1, \dots, n-1$ are n^2 area samples obtained from $P(x, y)$ with respect to regions A_{ij} , then the following relationship is satisfied

$$\iint_{A_{ij}} P(x, y) dx dy = F_{ij} \cdot S_{ij}, \quad i, j = 0, 1, \dots, n-1 \quad (2.2)$$

Where S_{ij} is the area of A_{ij} . Similarly, $P(x, y)$ in Eqn. (2.2) can be approximately represented by fitting points $P_{ij}, i, j = 0, 1, \dots, n-1$. By establishing mapping relationship between point samples P_{ij} and area samples $F_{ij}, i, j = 0, 1, \dots, n-1$ as shown in Eqn. (2.2), we can get approximations of point samples on surface $P(x, y)$.

In three-dimensional case: let $P(x, y, z)$ be a space body, and $F_{ijk}, i, j, k = 0, 1, \dots, n-1$ are n^3 area samples obtained from $P(x, y, z)$ with respect to regions Ω_{ijk} , then the following relationship is satisfied

$$\iiint_{\Omega_{ijk}} P(x, y, z) dx dy dz = F_{ijk} \cdot V_{ijk}, \quad i, j, k = 0, 1, \dots, n-1 \quad (2.3)$$

Where V_{ijk} is the volume of Ω_{ijk} . Similarly, $P(x, y, z)$ in Eqn. (2.3) can be approximately represented by fitting points $P_{ijk}, i, j, k = 0, 1, \dots, n-1$. Then, the mapping relationship between area samples F_{ijk} and point samples P_{ijk} is built. The computed $P_{ijk}, i, j, k = 0, 1, \dots, n-1$ are approximations of point samples on the space body $P(x, y, z)$.

2.2 CT Slice Segmentation

As discussed as above mapping relationship, we can get more accurate approximations of point samples on the original scene by constructing fitting curve/surface/volume to approximate the original scene. Due to the complexity of human anatomical structure as well as the irregularity and diversity of tissue organ, it is unreasonable to use the same curve/surface to fit data in different regions of raw CT slice. So, in our approach, we first segment the raw CT slice based on human tissue features, that is, divide the raw CT slices into different tissue regions. Then, in different regions, we fit the corresponding CT data respectively.

To segment the slice, the edges of the slice should be detected. There are many edge detection algorithms with various operators [5],[11]. It is important to note that slice segmentation in our approach aims at providing reasonable regions for latter fitting, not requires very accurate estimation of edge location. So we use Sobel operator to detect the edges of the CT slice. The Sobel operator, which is easier to calculate and less sensitive to noise, can produce better edge detection result with more accurate edge direction. The Sobel operator calculates the gradient of the image intensity at each pixel, if the magnitude

of the gradient vector achieves extremum, then the pixel is at the edge. The magnitude of gradient vector at pixel (x, y) can be computed by

$$M = \sqrt{s_x^2 + s_y^2} \quad (2.4)$$

Where s_x and s_y are the partial derivatives which can be implemented using two 3×3 convolution masks - one for horizontal changes, the other for vertical changes (as shown in Fig.2).

-1	0	1
-2	0	2
-1	0	1

-1	-2	-1
0	0	0
1	2	1

Fig. 2: Convolution masks: (a) Horizontal Convolution, (b) Vertical Convolution.

In our approach, the two convolution masks are convolved with the raw CT slice, and the gradient magnitude at each pixel is calculated using Eqn. (2.4). The resulted magnitude is compared with threshold, respectively. If the magnitude is greater than the threshold, then the corresponding pixel is at the edge of the CT slice and denoted as 1, otherwise as 0. All the 0 and 1 form the edge image. By searching the edge image, we can get different regions on raw CT slice.

As shown in Fig.3 (a), there are l raw slices in CT data field, each (denoted by blue) parallels to xy -plane and has n^2 pixels. Obviously, the CT data field can also be regarded as formed by n slices, each (denoted by red) parallels to yz -plane and has nl pixels, which we call X-CT slice in our approach to distinguish from the raw CT slice. The k^{th} CT slice and the j^{th} X-CT slice are shown in Fig.3 (b) and (c), respectively. With the requirement of latter spline fitting, we not only segment each CT slice with Sobel operator to get edge image (e.g., Fig.3 (d) is the edge image of the CT slice in Fig.3 (b)), but also segment each X-CT slice to get edge image.

2.3 Quadric Spline Fitting

2.3.1 Fitting idea

As described in section 1, each pixel corresponds to a voxel during CT scanning and is an area sample. As shown in Fig.3 (a), Let the density function of human body be $D(x, y, z)$, and pixels in the CT data field be F_{ijk} , $i, j = 0, 1, \dots, n-1, k = 0, 1, \dots, l-1$, then F_{ijk} can be regarded as the area sample of $D(x, y, z)$ in voxel. Assuming that the cube in Fig.4 is the voxel corresponding to pixel F_{ijk} in Fig.3 (b), P is the voxel center, the line L passes P and is perpendicular to yz -plane, the section S passes P and parallels to xy -plane. Then, based on the mapping relationship in Eqn.(2.3), F_{ijk} satisfies the following equation

$$\iiint_{\Omega_{ijk}} D(x, y, z) dx dy dz = F_{ijk} \cdot V_{ijk}, \quad i, j = 0, 1, \dots, n-1, k = 0, 1, \dots, l-1$$

Where Ω_{ijk} is the voxel, V_{ijk} is the volume of Ω_{ijk} . Let the coordinate of pixel F_{ijk} be (x_i, y_j, z_k) , then $\Omega_{ijk} = \left\{ (x, y, z) \mid x_{i-\frac{1}{2}} \leq x \leq x_{i+\frac{1}{2}}, y_{j-\frac{1}{2}} \leq y \leq y_{j+\frac{1}{2}}, z_{k-\frac{1}{2}} \leq z \leq z_{k+\frac{1}{2}} \right\}$. The center of voxel Ω_{ijk} is (x_i, y_j, z_k) .

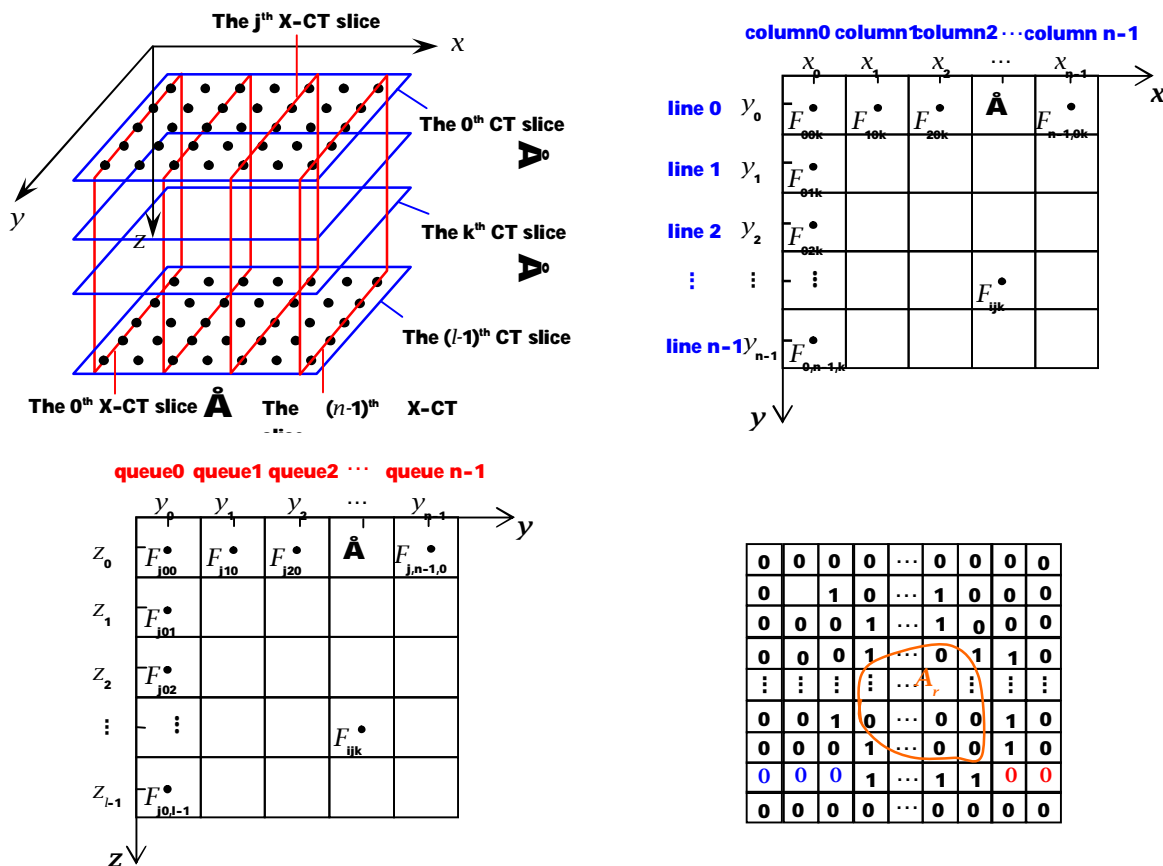


Fig. 3: Illustration of CT slice segmentation. The first row: (a) The CT data field, (b) The k^{th} CT slice; The second row: (c) The j^{th} X-CT slice, (d) The edge image of the k^{th} CT slice.

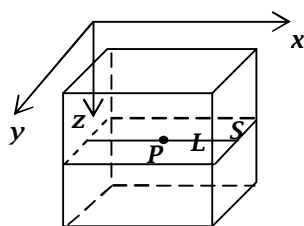


Fig. 4: The voxel Ω_{ijk} corresponding to the area sample F_{ijk} .

For simplicity, let voxel be unit cube, then, the above equation equals to

$$\int_{z_{k-\frac{1}{2}}}^{z_{k+\frac{1}{2}}} \int_{y_{j-\frac{1}{2}}}^{y_{j+\frac{1}{2}}} \int_{x_{i-\frac{1}{2}}}^{x_{i+\frac{1}{2}}} D(x, y, z) \, dx \, dy \, dz = F_{ijk}, \quad i, j = 0, 1, \dots, n-1, \quad k = 0, 1, \dots, l-1 \quad (2.5)$$

$D(x, y, z)$ in Eqn.(2.5) can be approximately represented by 3-dimensional quadric polynomial $P(x, y, z)$, which is constructed by fitting points P_{ijk} , $i, j = 0, 1, \dots, n-1, k = 0, 1, \dots, l-1$ as follows

$$P(x, y, z) = \sum_{k=0}^{l-1} \sum_{j=0}^{n-1} \sum_{i=0}^{n-1} \varphi_i(x) \varphi_j(y) \varphi_k(z) P_{ijk}$$

Substitute the above expression to Eqn.(2.5), we can get

$$\int_{z_{k-\frac{1}{2}}}^{z_{k+\frac{1}{2}}} \int_{y_{j-\frac{1}{2}}}^{y_{j+\frac{1}{2}}} \int_{x_{i-\frac{1}{2}}}^{x_{i+\frac{1}{2}}} \sum_{k=0}^{l-1} \sum_{j=0}^{n-1} \sum_{i=0}^{n-1} \varphi_i(x) \varphi_j(y) \varphi_k(z) P_{ijk} \, dx \, dy \, dz = F_{ijk}, \quad i, j = 0, 1, \dots, n-1, \quad k = 0, 1, \dots, l-1 \quad (2.6)$$

Eqn. (2.6) shows the relationship between area samples F_{ijk} and fitting points P_{ijk} , $i, j = 0, 1, \dots, n-1$, $k = 0, 1, \dots, l-1$. Here, P_{ijk} is the desired approximation of point sample at the voxel center (x_i, y_j, z_k) . Obviously, P_{ijk} can be obtained by solving Eqn. (2.6). Eqn. (2.6) includes n^2l unknown variables, and its solving process involves in large calculation and poor stability. Therefore, we decompose the solving process of the equation in Eqn. (2.6) to reduce calculation and improve stability. Let

$$U_{ij}(x, y, k) = \int_{y_{j-\frac{1}{2}}}^{y_{j+\frac{1}{2}}} \int_{x_{i-\frac{1}{2}}}^{x_{i+\frac{1}{2}}} \sum_{j=0}^{n-1} \sum_{i=0}^{n-1} \varphi_i(x) \varphi_j(y) P_{ijk} \, dx \, dy, \quad i, j = 0, 1, \dots, n-1 \quad (2.7)$$

where, $k = 0, 1, \dots, l-1$. Then, Eqn. (2.6) can be expressed as

$$\int_{z_{k-\frac{1}{2}}}^{z_{k+\frac{1}{2}}} \sum_{k=0}^{l-1} \varphi_k(z) U_{ij}(x, y, k) \, dz = F_{ijk}, \quad k = 0, 1, \dots, l-1 \quad (2.8)$$

where, $i, j = 0, \dots, n-1$. It can be seen that, the equation including n^2l unknown variables in Eqn. (2.6) is decomposed into n^2 equations in Eqn. (2.8), each equation includes l unknown variables. Obviously, each equation in Eqn. (2.8) reflects the mapping relationship in one-dimensional case as shown in Eqn. (2.1). Here, F_{ijk} can be regarded as area samples obtained from a curve along z -axis of the CT data field, and the curve can be approximated with a quadric polynomial curve constructed by the fitting points $U_{ij}(x, y, k)$, $k = 0, \dots, l-1$. Solving the equation can get $U_{ij}(x, y, k)$ from F_{ijk} . In Fig.4, the solving process of the equation equals to getting the average density of section S , i.e., the obtained $U_{ij}(x, y, k)$ is the average density of S . Similarly, let

$$V_i(x, j, k) = \int_{x_{i-\frac{1}{2}}}^{x_{i+\frac{1}{2}}} \sum_{i=0}^{n-1} \varphi_i(x) P_{ijk} \, dx, \quad i = 0, 1, \dots, n-1 \quad (2.9)$$

where, $j = 0, 1, \dots, n-1, k = 0, 1, \dots, l-1$. Then, Eqn. (2.7) can be expressed as

$$\int_{y_{j-\frac{1}{2}}}^{y_{j+\frac{1}{2}}} \sum_{j=0}^{n-1} \varphi_j(y) V_i(x, j, k) \, dy = U_{ij}(x, y, k), \quad j = 0, 1, \dots, n-1 \quad (2.10)$$

where, $i = 0, 1, \dots, n-1, k = 0, 1, \dots, l-1$, and $U_{ij}(x, y, k)$ has been obtained by Eqn. (2.8). From Eqn. (2.10), it can be seen that, the equation including n^2 unknown variables in Eqn. (2.7) is decomposed into n equations, each with n unknown variables. Similarly, each equation can be regarded as a curve along y -axis of the CT data field, which reflects the mapping relationship between area sample $U_{ij}(x, y, k)$ and point sample $V_i(x, j, k)$. Solving the equations can get $V_i(x, j, k)$. In Fig.4, the result of solving the equation is equivalent to getting the average density of Line L .

Similarly, assuming that $V_i(x, j, k)$ has been obtained in Eqn. (2.10), then Eqn. (2.9) can be expressed as

$$\int_{x_{i-\frac{1}{2}}}^{x_{i+\frac{1}{2}}} \sum_{j=0}^{n-1} \varphi_j(x) P_{ijk} dx = V_i(x, j, k), \quad i = 0, 1, \dots, n-1 \quad (2.11)$$

where, $j = 0, 1, \dots, n-1, k = 0, 1, \dots, l-1$. Each equation in Eqn. (2.11) has n unknown variables, and can be regarded as a curve along x -axis of the CT data field, which establishes the mapping relationship between area samples $V_i(x, j, k)$ and fitting points P_{ijk} . Solving the equations, we can get P_{ijk} , $i, j = 0, 1, \dots, n-1, k = 0, 1, \dots, l-1$, which are the desired approximations of point sample at the center of the voxels. In Fig.4, the result of solving the equation is equivalent to getting approximation of sample value at center P .

As described as above, by constructing a quadric fitting curve on each queue (along z -axis), each column (along y -axis) and each line (along x -axis) of the CT data field, more accurate approximations of point samples can be got. In our approach, quadric spline is used as the fitting curve for its simple expression, convenient calculation, and good fitting precision. It is important to note that, in section 2.2, CT slices and X-CT slices have been segmented into different regions. Thus, different quadric spline should be adopted to fit the pixels on the same line (or column, or queue) but in different segmented regions. For example, in Fig.3 (d), the pixels denoted by blue and red are on the same line but in different regions formed by segmenting CT slice, different quadric splines should be constructed to fit the blue and red pixels, respectively. Therefore, the basic idea of quadric spline fitting is: assuming F_{ijk} is in the region A_r formed by segmenting CT slices, as well as in the region A_s formed by segmenting X-CT slices. First, constructing quadric spline on each queue in the region A_s , then, constructing quadric spline on each line and each column in the region A_r , after the fitting process, more accurate approximations of point samples can be obtained from area samples F_{ijk} .

2.3.2 Fitting steps

The k^{th} CT slice and the j^{th} X-CT slice are shown in Fig.3 (b) and (c), respectively. Supposing that the pixels on the k^{th} CT slice are F_{ijk} , $i, j = 0, 1, \dots, n-1$, and each pixel coordinate is (x_i, y_j, z_k) , that is, the center of the square area corresponding to pixel is (x_i, y_j, z_k) . Obviously, pixel F_{ijk} is also on the j^{th} X-CT slice. The desired approximation of point sample at (x_i, y_j, z_k) is denoted by P_{ijk} , $i, j = 0, 1, \dots, n-1, k = 0, 1, \dots, l-1$. Obviously, the fitting sequence along x, y and z -axis has no effect on the results. So the steps of obtaining P_{ijk} , $i, j = 0, 1, \dots, n-1, k = 0, \dots, l-1$ are as follows:

Step 1. Each CT slice is processed in the following same way (take the k^{th} CT slice for example).

1) Detect the edges of the k^{th} CT slice with Sobel operator to get edge image M_k .

2) Construct quadric spline on each line of the k^{th} CT slice, i.e. along x -axis of the CT data field, to establish the mapping relationship between area samples and point samples. In the spline fitting process, edge image M_k is checked. If the pixels are on the same line but in different segmented regions, different quadric splines should be adopted to fit them (the fitting details are described in section 3). Take pixels on the i^{th} line for example, a quadric spline P_{r1} is constructed to fit the ones in region A_{r1} , and another quadric spline P_{r2} is constructed to fit the ones in A_{r2} , and so on. After fitting, the transition values P''_{ijk} at (x_i, y_j, z_k) on the k^{th} CT slice can be got from F_{ijk} , where, $i, j = 0, 1, \dots, n-1$.

3) Using P''_{ijk} , $i, j = 0, 1, \dots, n-1$ obtained in 2) as area samples, construct quadric spline on each column of the k^{th} CT slice, i.e., along y -axis of the CT data field. Similarly, edge image M_k is checked in the spline fitting process, and different quadric splines should be adopted if the pixels are on the same column but in different segmented regions. After fitting, the transition values P'_{ijk} at (x_i, y_j, z_k) on the k^{th} CT slice can be got from P''_{ijk} , $i, j = 0, 1, \dots, n-1$.

Step 2. Each X-CT slice is processed in the following same way (take the j^{th} X-CT slice for example).

1) Detect the edges of the j^{th} X-CT slice to get edge image M_j .

2) Construct quadric spline on each queue of the j^{th} X-CT slice, i.e., along z -axis of the CT data field. In the spline fitting process, edge image M_j is checked, and different quadric splines should be adopted if the pixels are on the same queue but in different segmented regions. After fitting, P_{ijk} at (x_i, y_j, z_k) on the j^{th} X-CT slice can be got from P'_{ijk} , $i = 0, 1, \dots, n-1, k = 0, 1, \dots, l-1$.

P_{ijk} obtained during the above process is the desired more accurate approximation of point sample at (x_i, y_j, z_k) , where, $i, j = 0, 1, \dots, n-1, k = 0, 1, \dots, l-1$.

The principle and process of quadric spline fitting on each line, each column, and each queue are the same. So, in the following section, we only describe the details in quadric spline fitting on a line.

3 THE LINE QUADRIC SPLINE FITTING

3.1 Basic Idea

Take the i^{th} line on the k^{th} CT slice for example. We only discuss the process of fitting the pixels on the i^{th} line as well as in the segmented region A_i (as shown in Fig.3 (d)). The process of fitting other pixels on the i^{th} line is the same. Assuming there are t pixels on the i^{th} line as well as in A_i and the area samples are $F_{ijk}, i = s_0, \dots, s_{t-1}$. By adopting quadric spline to establish the mapping relationship between area samples and point samples, we can get approximations of point sample at $(x_i, y_j, z_k), i = s_0, \dots, s_{t-1}$. These approximations will be used in the latter quadric spline fitting on each column and each queue. Obviously, all the y and z -axis of the pixels on the i^{th} line are the same, and the mapping relationship is in one-dimensional case. For convenience of description, the area sample (i.e., pixel) on the i^{th} line as well as in A_i is denoted as $T_i, i = 0, 1, \dots, t-1$, and its x coordinates is denoted as x_i . $[x_{i-\frac{1}{2}}, x_{i+\frac{1}{2}}]$ is the unit region centered at x_i . The approximations of point sample at x_i is denoted as $P_i, i = 0, 1, \dots, t-1$. The basic idea of obtaining P_i from $T_i, i = 0, 1, \dots, t-1$ is as follows:

1. Construct a quadric spline $P(x)$ using $P_i, i = 0, 1, \dots, t-1$.

2. Based on the mapping relationship in Eqn. (2.1), integrate $P(x)$ on each region $[x_{i-\frac{1}{2}}, x_{i+\frac{1}{2}}]$, and make the integral equal to product of T_i and the length of $[x_{i-\frac{1}{2}}, x_{i+\frac{1}{2}}]$, $i = 0, 1, \dots, t-1$. These integral equations establish the relations among P_i, M_i and $T_i, i = 0, 1, \dots, t-1$. Where, M_i is the second derivative of $P(x)$ at x_i , respectively.

3. Combine the relations among P_i , M_i and $T_i, i = 0, 1, \dots, t-1$ with the continuity conditions and boundary conditions of $P(x)$, in order to get the M -continuity equations of $P(x)$. Solving the M -continuity equations can get $M_i, i = 0, 1, \dots, t-1$, and then, get $P_i, i = 0, 1, \dots, t-1$.

3.2 Specific Steps

Step 1. Supposing that the first and the second derivative at x_i are m_i and M_i , respectively, where, $i = 0, 1, \dots, t-1$, then a quadric spline $P(x)$ is constructed in the interval $[x_0, x_{t-1}]$. Let $P(x)$ be denoted as $P_i(x)$ on the short interval $[x_{i-\frac{1}{2}}, x_{i+\frac{1}{2}}]$, $i = 0, 1, \dots, t-1$, then

$$P_i(x) = P_i + m_i(x - x_i) + \frac{1}{2}M_i(x - x_i)^2, \quad i = 0, 1, \dots, t-1$$

Step 2. Integrate $P(x)$ on each region $[x_{i-\frac{1}{2}}, x_{i+\frac{1}{2}}]$, $i = 0, 1, \dots, t-1$, respectively. Here, $[x_{i-\frac{1}{2}}, x_{i+\frac{1}{2}}]$ is unit region. Then

$$\int_{x_{i-\frac{1}{2}}}^{x_{i+\frac{1}{2}}} P(x) dx = \int_{x_{i-\frac{1}{2}}}^{x_{i+\frac{1}{2}}} P_i(x) dx = P_i + \frac{1}{48}M_i, \quad i = 0, 1, \dots, t-1 \quad (3.1)$$

Based on the mapping relationship between area samples and point samples in Eqn. (2.1), we get

$$\int_{x_{i-\frac{1}{2}}}^{x_{i+\frac{1}{2}}} P(x) dx = T_i, \quad i = 0, 1, \dots, t-1 \quad (3.2)$$

From Eqns.(3.1)-(3.2), we can get the relations among P_i , M_i and $T_i, i = 0, 1, \dots, t-1$ as follows

$$P_i = T_i - \frac{1}{24}M_i, \quad i = 0, 1, \dots, t-1 \quad (3.3)$$

Step 3. According to the quadric spline property, $P(x)$ satisfies the following continuity conditions

$$P_i(x_{i+\frac{1}{2}}) = P_{i+1}(x_{i+\frac{1}{2}}), \quad P_i'(x_{i+\frac{1}{2}}) = P_{i+1}'(x_{i+\frac{1}{2}}), \quad i = 1, 2, \dots, t-2 \quad (3.4)$$

From Eqn.(3.4), M -continuity equations of $P(x)$ can be got

$$M_{i-1} + 6M_i + M_{i+1} = 8(P_{i-1} - 2P_i + P_{i+1}), \quad i = 1, 2, \dots, t-2 \quad (3.5)$$

From Eqns.(3.3) and (3.5), we get

$$M_{i-1} + 4M_i + M_{i+1} = 6(T_{i-1} - 2T_i + T_{i+1}), \quad i = 1, 2, \dots, t-2 \quad (3.6)$$

Based on imitation of manual lofting, the boundary conditions are given as follows

$$4M_0 + M_1 = 6(T_1 - 2T_0), \quad M_{t-2} + 4M_{t-1} = 6(T_{t-2} - 2T_{t-1}) \quad (3.7)$$

Eqns.(3.6) and (3.7) constitute the complete M -continuity equations of $P(x)$ whose matrix expression

Fig.5 shows the comparison of 3D reconstructed results generated by different reconstruction algorithms based on the CT data before and after optimization with our approach. The data consist of 140 lung CT slices whose resolution is 512×512 . For convenience of description, the 140 raw CT slices before optimization are named raw data, and the data obtained by optimizing the raw CT data with our approach are named new data. Fig.5 (a) and (b) are the reconstructed results with SSD (Shaded Surface Display) method. Here, we use the classical marching cubes algorithm in [9] as the SSD method. The data used for reconstruction in Fig.5 (a) and (b) are different. Fig.5 (a) uses the raw data, and Fig.5 (b) uses the new data, but all other parameters in SSD are the same in Fig.5 (a) and (b). Fig.5 (c) and (d) are the reconstructed results with MIP (Maximum Intensity Projection) method. Fig.5 (c) uses the raw data, and Fig.5 (d) uses the new data. All other parameters in MIP are the same in Fig.5 (c) and (d).

It can be seen from the comparisons in Fig.5 that, when the same reconstruction algorithm is respectively conducted on the raw data and the new data, the 3D reconstructed image based on the new data is better. It demonstrates that the precision of the CT data per se is improved after optimization, and consequently, the detail information of the 3D image reconstructed on the optimized data increases evidently. Some improved details are marked by small circles in Fig.5. Additionally, some artifacts in image are eliminated. For example, the artifacts denoted by yellow rectangles in Fig.5 (a) are eliminated in Fig.5 (b). Fig.5 shows that our approach has high precision because the precision of the reconstruction with the new data are significantly improved.

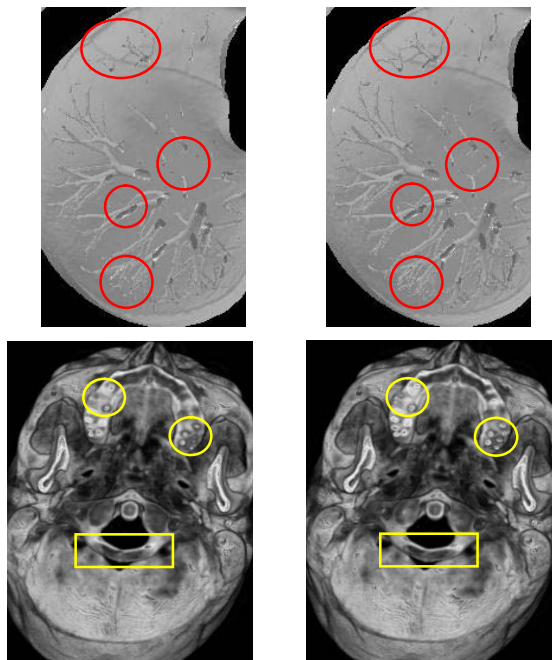


Fig. 6: Visual comparison of reconstructed results based on different groups of CT data. The first row: (a) and (b) are the results of reconstructing 90 slices of lung CT data with SSD method. (a) is the reconstruction on the raw data, and (b) is the reconstruction on the new data optimized by our approach. The second row: (c) and (d) are the results of reconstructing 100 slices of head CT data with VRT method. (c) is the reconstruction on the raw data, and (d) is the reconstruction on the new data optimized by our approach.

Fig. 6 shows the comparison of 3D reconstructed results generated by different reconstruction algorithms based on different CT data. The data in Fig.6 (a) and (b) consist of 90 lung CT slices whose resolution is 512×512 , and the same SSD method as in Fig.5 is used for reconstruction. Fig.6 (a) uses the raw data and Fig.6 (b) uses the new data obtained by optimizing the raw data. The data in Fig.6 (c) and (d) consist of 100 head CT slices whose resolution is 512×512 , and VRT (Volume Rendering Technology) method is used for reconstruction. Here, we use the shear-warp algorithm in [7] as the VRT method. Fig.6 (c) uses the raw data and Fig.6 (d) uses the new data. Some improved details are marked by small circles in Fig.6. It can be seen that, the precision of 3D reconstruction with the new data is much higher than that with the raw data, demonstrating that our approach has high optimization precision.

Fig.7 shows visual comparison of 3D images reconstructed respectively on the CT data before and after optimization with our approach. Here, we use the algorithm in [8] for volume rendering. The data in Fig.7 (a) and (b) consist of 110 lung CT slices whose resolution is 512×512 . Fig.7 (a) is the result reconstructed on the raw data, and Fig.7 (b) is the result reconstructed on the new data obtained by optimizing the raw data. The data in Fig.7 (c) and (d) consist of 80 head CT slices whose resolution is 512×512 . Fig.7 (c) is the result reconstructed on the raw data, and Fig.7 (d) is the result reconstructed on the new data. It can be seen from these comparisons that, when the same algorithm is used for 3D reconstruction, the reconstruction quality on the new data optimized by our approach is better (some improved details are marked by small circles), demonstrating the efficiency of our approach for improving the CT data precision.

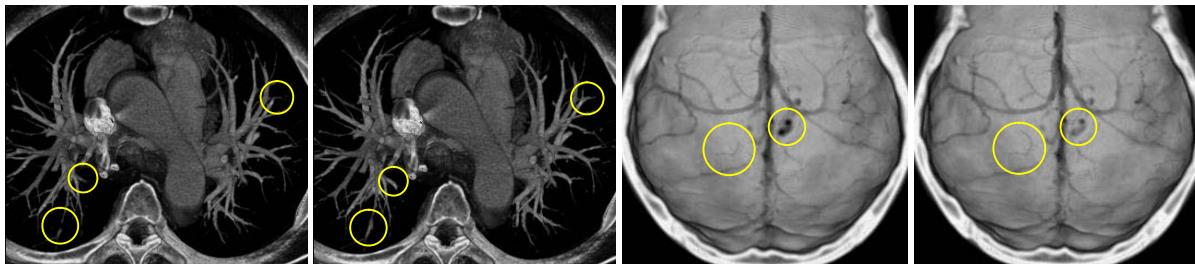


Fig. 7: Visual comparison of 3D images reconstructed on the CT data before and after optimization. (a) The result reconstructed on the lung raw data, (b) The result reconstructed on the new data obtained by optimizing the lung raw data, (c) The result reconstructed on the head raw data, and (d) The result reconstructed on the new data obtained by optimizing the head raw data.

5 CONCLUSIONS

Based on the fact that the raw CT data acquired with scanner can be regarded as area samples, we present a new approach for optimizing CT data precision in this paper. The new approach transforms these area samples to more accurate approximations of point samples to improve the precision of the CT data per se. Utilization of these new optimized CT data for 2D rendering or 3D reconstruction can improve the reconstruction quality, and reduce the reconstruction errors. Additionally, in single-layer showing, it only needs to conduct quadric spline fitting on each line and each column of the CT slice as do as in the step1 of our approach, and then use the new optimized data to render. When 3D volume rendering or surface rendering is needed, it should conduct the whole fitting procedure, in order to achieve better reconstruction precision.

ACKNOWLEDGEMENTS

This work is supported by Projects of International Cooperation and Exchanges NSFC under grant 61020106001, Nature Science Foundation of Shandong Province under grant ZR2010FQ031, ZR2010FQ025, and Jinan Youth Star Program under grant 201101-0113.

REFERENCES

- [1] Kalvin, A. D.; Laine, A. F.; Song, T.: Faster, higher quality volume visualization for 3d medical imaging, Proc. SPIE, v 6918, 2008, #30. DOI: 10.1117/12.770990
- [2] Avinash, C. K.; Malcolm, S.: Principles of Computerized Tomographic Imaging, Society for Industrial and Applied Mathematics, Philadelphia, 2001. DOI: <http://dx.doi.org/10.1137/1.9780898719277>
- [3] Dilmaqhani, R. S.; Ahmadian, A.; Maleki, N.: Choice of wavelet filters for medical image compression and approximation, Proc. Annual International Conference of the IEEE Engineering in Medicine and Biology, v. 2, 2002, 1059-1060. DOI: 10.1109/IEMBS.2002.1106275
- [4] Chernyaev, E. V.: Marching cubes 33: construction of topologically correct isosurfaces, Technical Report CERN CN 95-17, CERN, 1995, DOI: 10.1.1.56.7139
- [5] Gonzalez, R. C.; Woods, R. E.: Image Processing, Second Edition, Publishing House of Electronics Industry, Beijing, 2003, 463-474.
- [6] Grevera, G. J.; Udupa, J. K.; Miki, Y.: A task-specific evaluation of three-dimensional image interpolation techniques, IEEE Transactions on Medical Imaging, 18(2), 1999, 137-143. DOI: 10.1109/42.759116
- [7] Schulze, J. P.; Kraus, M.; Lang, U.; Ertl, T.: Interacting pre-integration into the shear-warp algorithm, proceedings of the 2003 Eurographics/IEEE TVCG Workshop on Volume graphics, 2003, 109-118. DOI: 10.1145/827051.827068
- [8] Choi, K.-Y.; Jo, S.-U.; Jeong, C.-S.: New optimization techniques for shear-warp volume rendering, Future Information Technology, 185(5), 2011, 425-422. DOI: 10.1007/978-3-642-22309-9_56
- [9] Thomas, L.; Hélio, L.; Antonio, M. V.; Geovan, T.: Efficient implementation of marching cubes cases with topological guarantees, Journal of Graphics Tools, 8(2), 2003, 1-15. DOI: 10.1.1.2.8509
- [10] Goldman, L. W.: Principles of CT and CT technology, Journal of Nuclear Medicine Technology, 35(3), 2007, 115-128. DOI: 10.2967/jnmt.107.042978
- [11] Sharifi, M.; Fathy, M.; Mahmoudi, M. T.: A classified and comparative study of edge detection algorithms, Proceedings of International Conference on Information Technology: Coding and Computing, 2002, 117-120. DOI: 10.1109/ITCC.2002.1000371
- [12] Lacroute, P.; Levoy, M.: Fast volume rendering using a shear-warp factorization of the viewing transformation, SIGGRAPH, 1994, 451-458. DOI: 10.1145/192161.192283
- [13] Thévenaz, P.; Blu, T.; Unser, M.: Interpolation Revisited, IEEE Transactions on Medical Imaging, 19(7), 2000, 739-758. DOI: 10.1109/42.875199
- [14] Qian, F.; Ma, X L.; Wan W Q.; Zhang J Q.: A novel surface rendering algorithm for 3D reconstruction of medical images, Proc. CCWMC, 2009, 484-487. DOI: 10.1049/CP.2009.1996
- [15] Ramani, S.; Thevenaz, P.; Unser, M.: Regularized interpolation for noisy images, IEEE Transactions on Medical imaging, 29(2), 2010, 543-558. DOI: 10.1109/TMI.2009.2038576
- [16] Rares, A.; Reinders, M. J. T.; Biemond J.: Edge-based image restoration, IEEE Transactions on Image Processing, 14(10), 2005, 1454-1468. DOI: 10.1109/TIP.2005.854466

- [17] Shi, J. Z.; Reichenbach, S. E.: Image interpolation by two-dimensional parametric cubic convolution, *IEEE Transactions on Image Processing*, 15(7), 2006, 1857-1870. DOI: 10.1109/TIP.2006.873429
- [18] Lehmann, T. M.; Gönner, C.; Spitzer, K.: Survey: interpolation methods in medical image processing, *IEEE Transactions on Medical Imaging*, 18(11), 1999, 1049-1075. DOI: 10.1109/42.816070
- [19] Möller, T.; Mueller, K.; Kurzion, Y.; Machiraju, R.; Yagel, R.: Design of accurate and smooth filters for function and derivative reconstruction, *Proc. IEEE Symposium on Volume Visualization*, 1998, 143-151. DOI: 10.1109/SVV.1998.729596
- [20] Tsai, M.-D.; Hsieh, M.-S.: Surface rendering for multi-axial cross sections, *Journal of Information Science and Engineering*, 17(1), 2001, 113-132. DOI: http://www.iis.sinica.edu.tw/page/jise/2001/200101_08.html
- [21] Wang, Ch. H.; Liu, Y C.; Zhang W B.; Shen G F.: Study on 3D reconstruction of medical image and orthographic views, *Proc. BMEI*, 2009, 1-4. DOI: 10.1109/BMEI.2009.5305802
- [22] Weber, G. H.; Dillard, S. E.; Carr, H.; Pascucci, V.; Hamann, B.: Topology-controlled volume rendering, *IEEE Transactions on Visualization and Computer Graphics*, 13(2), 2007, 330-341. DOI: 10.1109/TVCG.2007.47
- [23] Zhang, X. Q.; Wu, X. L.: Image interpolation by adaptive 2-D autoregressive modeling and soft-decision estimation, *IEEE Transactions on Image Processing*, 17(6), 2008, 887-896. DOI: 10.1109/TIP.2008.924279